THE BØIFOT ORTHOMODE JUNCTION

E.J. Wollack[1], W. Grammer[2], and J. Kingsley[2]

National Radio Astronomy Observatory[2]
949 North Cherry Avenue, Tucson, AZ 85721

Laboratory for Astronomy and Astrophysics[1]
NASA/Goddard Space Flight Center
Greenbelt, MD 20771
email: edward.wollack.1@gsfc.nasa.gov

***Abstract* — Wideband dual-polarization performance is desired for low-noise receivers and radiometers at centimeter and millimeter wavelengths. The use of a waveguide orthomode transducer (OMT) can increase spectral coverage and sensitivity while reducing exit aperture size, optical spill, and instrumental polarization offsets. For these reasons, an orthomode junction is favored over a traditional quasi-optical wire grid for focal plane imaging arrays from a systems perspective. The fabrication and performance of wideband symmetric Bøifot OMT junctions at K-, Ka-, Q-, and W-bands are described. Typical WR10.0 units have an insertion loss of <0.2 dB, return loss ~20dB, and >40dB isolation over a >75-to-110 GHz band. The OMT operates with reduced ohmic losses at cryogenic temperatures.**

Keywords: Orthomode Transducer, Orthomode Junction, Polarization Diplexer, Waveguide Techniques

INTRODUCTION:

Receiver systems for radioastronomy and other precision low-noise applications require high-performance polarization-discrimination components. For dual-polarization operation, it is desirable for the cross-polarization induced by the OMT to be stable and less than the level arising from the feed assembly and telescope. Optimization of the total optical efficiency over a standard single-mode rectangular waveguide bandwidth is desirable for compatibility with present low-noise receiver designs. At cryogenic temperatures, ohmic losses in the OMT are not a great limitation; however, it is desirable to minimize mode conversion in order to mitigate and control transmission resonances in the feed assembly. To achieve these goals, a highly symmetric feed and OMT structure is necessary.

Asymmetric OMTs have been commonly used for polarization diplexing in microwave applications. The performance of these structures is limited in practice to a fractional bandwidth of ~10-to-20% by the excitation of higher-order modes in the common-arm. Historically, these designs were driven by a desire to minimize the volume, mass, and transmission loss incurred in achieving polarization discrimination. For a survey of narrow band OMT designs see Ragan (1948), Harvey (1963), and Smullin and Montgomery (1948).

Symmetric OMTs designs enable the use of a fractional bandwidth of >40% by controlling the excitation of higher-order modes in the structure. The fin-line OMT investigated by Robinson (1956) and revisited by Chattopadhyay and Carlstrom (1998) is an inherently wideband design of interest in the short wavelength limit. Performance of the symmetric dual-ridge and fin-line designs can be found in Skinner and James

(1991). The mechanically asymmetric full waveband design by Steffe (1995) is novel in its use of discontinuities to realize a broadband conjugate impedance match at microwave wavelengths. The turnstile junction developed at the MIT Radiation Laboratory during World War II by R. Dicke is a natural candidate for wideband performance as a result of its fourfold symmetry. A summary of turnstile applications in rectangular-guide is given by Meyer and Goldberg (1955). Gehin and Tourneur (1986) describe a wideband ridge-guide turnstile OMT junction. However, the structure is inherently three dimensional and presents manufacturing challenges in the high frequency limit. Also, see Uher, et al. (1993) for a comprehensive review of wide and narrow-band OMT designs used in communication applications.

The twofold symmetric junction introduced by Bøifot (1990) was chosen as the starting point for the orthomode junctions designs investigated here. This symmetric OMT achieves full waveguide band performance by limiting the excitation of TE_{11} and TM_{11} in the square common-port. The principal innovation of this approach is that the component can be manufactured as a split-block with conventional numerically-controlled machining techniques. These properties have lead to its use in full-waveguide band receivers at centimeter and millimeter wavelengths (Cazzatello et al., 1996; Wollack, 1996). More recently, variations on these ideas have been explored with machinable apertures replacing the discrete compensation pins (Nesti, 2002; Narayanan & Erickson, 2002).

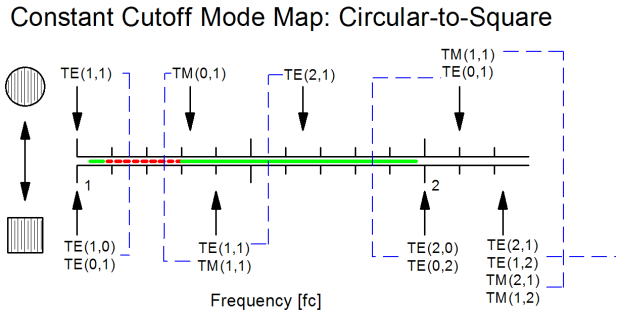

THE BØIFOT JUNCTION:

The Bøifot OMT can be viewed as a variant on the turnstile junction where two of the ports have been folded parallel to the common-port. See Figure 1. The two ports that form the main-arm are separated by a thin septum, combined, and transformed to standard-height waveguide. For the other polarization, this septum forms a pair of back-to-back "mitred'" bends which feed the symmetric side-arm ports. The pin number, diameter, and location are a compromise between tuning the septum reactance produced in the side-arm ports and allowing a low impedance return path for the main-arm currents. From the perspective of the main-arm, it is useful to think of the pins as a pair of short-circuited waveguide-stubs used to tune out the discontinuity due to side-arm junctions. The signal coupled to the side-arms is transformed with an adiabatic taper and recombined. The side-arms can be thought of as a "thick septum" from which the main-arm is carved. This configuration allows the use of relatively compact and wideband E-plane bends and power combiners. At each junction in the structure, to lowest order, the impedance is constant, however, other implementations can be envisioned. The main and side-arm junctions are twofold symmetric about the horizontal and vertical guide planes, thus, TE_{11} and TM_{11} excitation can be avoided in the square common-arm of the junction to the extent this condition is realized in fabrication of the assembly.

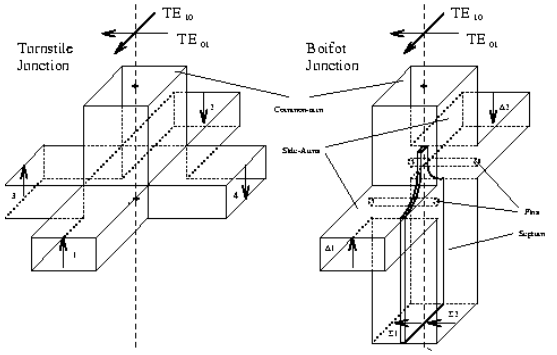

Figure 1: Turnstile and Bøifot Waveguide Junction Geometries

The junction's control over modal symmetry is of considerable importance for orthomode transducer performance. The common-arm supports six modes over a standard 2:1 rectangular waveguide band – only two of which are desired for propagation. The bandwidth of the isolation and match are essentially determined by the excitation of higher-order modes. Since both polarizations must propagate in the common-arm, the higher-order mode's cutoff frequencies are lower than the upper-band-edge. Most of the modes in the structure are evanescent and thus do not propagate; however, if excited, the resulting reactance must be compensated. The remaining modes are controlled by careful definition of the junction symmetry. The isolation is ultimately determined by the level of modal conversion, the septum length, and

achieved symmetry. In addition, alignment of the common-arm guide is also critical to minimize excitation of TE_{11} and TM_{11} at the flange interface. We now consider the detailed function of each element of the OMT in detail:

Side-Arm Transitions: When illuminating the junction with the polarization which couples to the side-arm port, the septum appears as two back-to-back miters which act as a power divider. The main-arm appears as a dispersive reflective termination. The pin/septum geometry provides a double-tuned match which is sensitive to small perturbations in the geometry. The length and width of the septum tips are varied to produce the resonance at the upper/lower band edges. We have studied and fabricated designs with septa thicknesses in the range of $0.02 < dt_{septum}/a_o < 0.05$, where dt_{septum} is the septum thickness and a_o is the broadwall dimension. In general, the thinner the septa, the easier the structure is to compensate, however, HFSS (High-Frequency-Structure-Simulator) [16] simulations indicate that suitable compensation can be realized for thicker septa if desired. For modeling and design purposes, we consider $1.2 < f/f_c < 1.9$ as the design band, where f_c is the guide cutoff frequency.

The side-arm bends and impedance transformers are a compromise between ohmic and return loss. In addition, they must be the same electrical path length for the side-arm signals to correctly recombine. This can be seen by considering the limit where one arm experiences a phase shift of 180° with respect to the other and the signals cancel at the power combiner output. Due to the length of the side-arms, such a phase error manifests itself as constructive/destructive interference or "beating" between the signals at the side-arm output. This will also occur if the upper and lower split-blocks are not precisely aligned in the side-arm septum region. The side-arm power combiner septum is compensated for minimal reflection and employs adiabatic transformation in guide height to match the output guide size. The Hecken impedance profile employed is defined in Appendix "A".

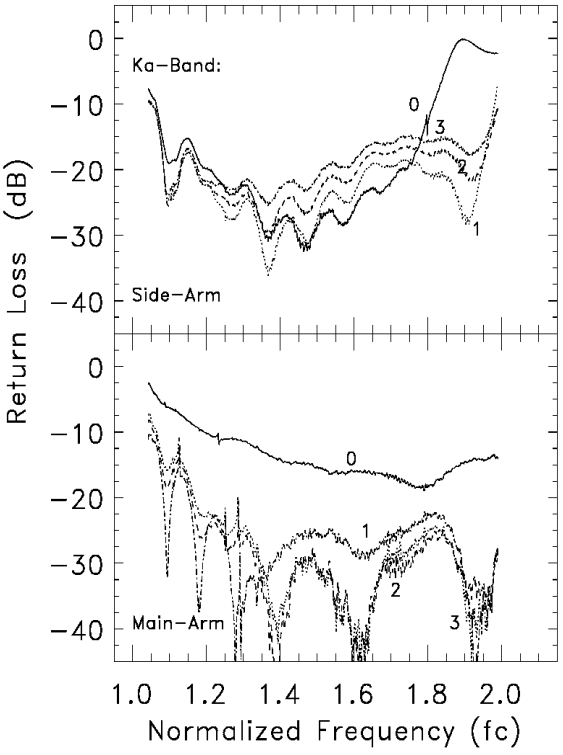

Figure 2: Side/Main-Arm Frequency Response; Parameter Compensation Pin Number and Location.

Main-Arm Transition: When illuminating the junction with the polarization which couples to the main-arm port, the pins act as symmetric short-circuit waveguide-stubs which tune out the discontinuity due to the side-arm ports. With two pins in each aperture, the return loss is minimized when the pins are centered in the aperture formed by the side-arm wall. Pins in the range, $0.05 < 2d_{pin}/a_o < 0.07$, provide a nice compromise between the main- and side-arm return loss requirements. With one pair of pins, the optimal position occurs with the outer diameter of the pin is flush to the side-arm wall (i.e., the pins are physically in the common-arm) and centered in the side-arm aperture. As demonstrated in Figure 2, as the total number of pins is increased from zero to the three pairs described, the main-arm return loss improved while the side-arm gracefully degrades. The septum tip forms an adiabatic impedance transformer from 1:1 guide to $(1-dt_{septum}/a_o)$:1. This is followed by a four-step, 2:1 Tchebyshev impedance transformer with a normalized fractional bandwidth of $w_q = 0.84$, and synchronous frequency of $f_o/f_c=1.565$ [17]. A compensated E-plane bend is used to redirect the transformer output and avoid interference with the side-arm guides.

Main-Arm Miter Bend: For designs at wavelengths >10mm; angled miter, single-step, and double-step compensation designs have been considered for the main-arm bend. In principle, the match can be improved by increasing the number of discontinuities in the miter junction [18,19], however, the contribution to the main-arm return loss does not present a fundamental limitation for the designs

considered. Due to the sensitivity of such a miter junction's response to relatively small dimensional errors, this increase in manufacturing complexity is unlikely to be commensurate with the performance improvement. For designs at wavelengths <10mm, from a manufacturing perspective it is highly desirable to avoid having the compensation protrude above the split plane of the block. This allows the block to be lapped or surface ground to achieve the flatness and finish for proper mating of the two halves of the block, avoids the formation of a gap in the vicinity of the critical miter region, and reduces the required mechanical tolerances. In the limit the junction is smaller than the necessary hardware required to mate the flange, consideration of a single step compensated bend (i.e., a height and width equal to $b_o/2$, [20]) can simplify mounting by eliminating the blind holes for the main-arm flange. At microwave frequencies, the main-arm miter is typically replaced by a waveguide launcher to reduce the overall envelope.

Side/Main-Arm Layout Considerations: The angles that the side-arms meet the common-arm-junction and are subsequently recombined at the power combiner are largely a matter of packaging convenience. For example, in Bøifot's original design 90°/0° angles were respectively employed in the layout of the split-block (e.g., see Figure 9). This choice for the side-arm power combiner is not ideally suited for millimeter wavelengths due to the necessity to machine a thin free-standing septum in each block. Increasing the side-arm power combiner angle to 90° opens up the region in the vicinity of the main-arm for flange screws in the long wave length limit (i.e., the screws reside inside the side-arm guide perimeter). A back-to-back 45° miter compensation for the combiner reduces the difference in path length between the side- and main-arms. The choice 45°/45° for the junction and power combiner angles (e.g., see Figure 7) minimizes the overall envelop and loss of the OMT, maximizes the available volume for the common-arm flange screws, and allows the main-arm flanges screws to span the side-arm guide perimeter in the high frequency limit. For ease of manufacture for the bands presently under consideration, we find 90°/45° (e.g., see Figures 6 and 8) as a reasonable compromise between the flanging interface requirements and equalizing the ohmic loss incurred by the signal between the side- and main-arm ports.

In contrast to the microwave limit, where a premium is placed upon reduction of the volume and mass, as one goes to millimeter wavelengths; insensitivity to tolerance and low loss tends be the overriding design consideration. In this limit, unless a high level of component integration is achieved, the mechanical requirements to realize a precision flange mate tend to dictate the overall size of the device.

Side-Arm Power Combiner: Compensation for the side-arm waveguide power combiner is simplified by taking advantage of symmetry ([21], section 12.16). Consider the three-port in Figure 3. For the case $\alpha_1 = \alpha_2 \sim 0$, if the septum thickness is small compared to the guide height, insertion (or removal) of the septum does not adversely affect the field distribution of the dominant mode; it merely defines a junction symmetry plane. If the septum's thickness is non-zero, the resulting capacitive discontinuity must be compensated to achieve a broadband response at port one. A lossless reciprocal three-port cannot present three matched ports simultaneously. If one desires to match port one, $S_{11} \sim 0$, ports two and three should be terminated into well-matched loads. The coupling between port one and port two or three in this limit is 3dB, and the resultant isolation from ports two to three is 6dB.

We recall that the frequency sensitivity is minimized to the extent that the total stored energy is the same for all junction eigen-solutions [21]. This would suggest the following design rules are desirable to achieve broadband response: 1) The dominant mode symmetry should be preserved by junction geometry; 2) The guide heights of the three ports are linked by the power division ratio, $R = b_1/b_2$ and the desire to minimize the frequency dependence of the junction discontinuities, $b_o = b_1 + b_2$; 3) The shaded region in Figure 2 is a perfect E-wall. Thus, any element which compensates a compact bend in the spirit of De Ronde [22] can achieve the desired match by consideration of the junction's electromagnetic symmetry under reflection and rotation.

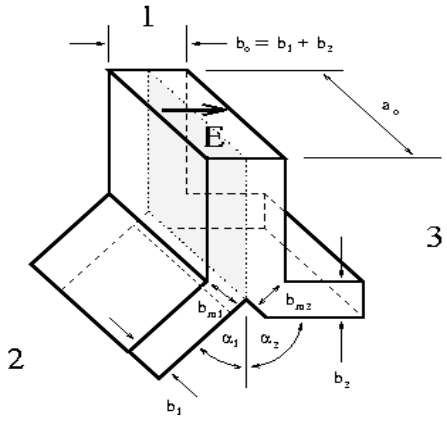

Figure 3: Generalized Bi-Furcation Waveguide Power Combiner Geometry.

This symmetry allows the use of optimal miter and other bend designs to be used for the compensation of the power combiner junction. A list of typical examples is given in Table 1. HFSS simulations for these geometries are shown in Figure 4 and indicate that a ~35dB return loss is readily achievable. In practice, cases "A", "B", and "C" have been found to have indistinguishable electrical response; however, design "B" is preferred from a fabrication standpoint. Since the power combiner is fabricated as an E-plane split-block by conventional milling techniques, we note the following: 1) The cutting depth is limited to ~3 times the tool outer diameter, OD. 2) The cutter diameter must clear the compensation region. In this case, the tool diameter is restricted to lie in the range: $a_o/6 < OD < b_m$. This approach yields a variety of wideband designs which are robust and degrade gracefully with dimensional errors which can be used optimize the layout of the side-arm guides [23].

Case	α_1	α_2	a_o:b_o	a_o:b_1	a_o:b_2	b_{m1}/b_1	b_{m2}/b_2
A	0	0	2:1	4:1	4:1	1.00	1.00
B	π/4 π/4	π/4 π/4	2:1 1:1	4:1 2:1	4:1 2:1	0.93 0.92	0.93 0.92
C	π/2	π/2	2:1	4:1	4:1	0.84	0.84
D	π/4	π/2	2:1	4:1	4:1	0.93	0.84
E	0	π/2	2:1	4:1	4:1	1.00	0.84
F	0	π/4	2:1	4:1	4:1	1.00	0.93
G	π/2	π/2	2:1	4:1	4:1	1-step	1-step
H	π/2	π/2	2:1	4:1	4:1	2-step	2-step

Table 1: E-Plane Waveguide Power Combiner Geometry

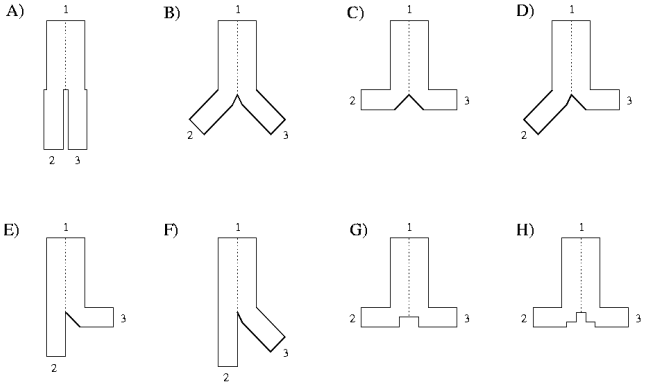

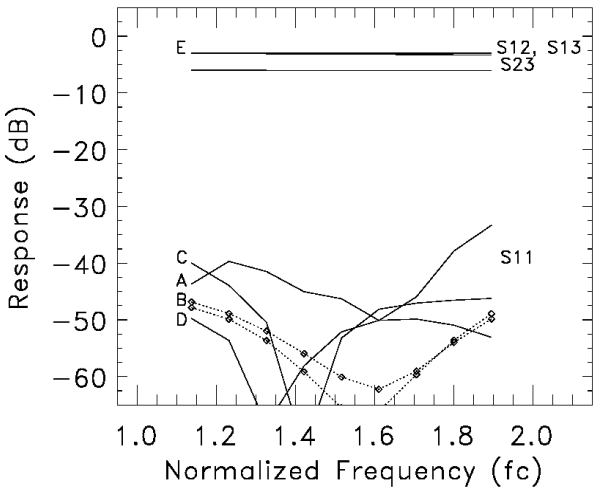

Figure 4: Power Combiner Modeled Responses for a Selection of Compensation Geometries. The asymmetry between S_{12} and S_{13} indicated is the worst case encountered (test case "E"; $\alpha_1 \neq \alpha_2$). Designs with unequal power division, $b_1 \neq b_2$, result in similar discrepancies.

Summary.

A DETAILED EXAMPLE: ALMA BAND-3 OMT

As an explicit Bøifot junction example, we consider the ALMA Band-3 OMT depicted in Figure 5. This design was optimized to interface with the NRAO SIS mixer block design (c.a. ~1997). The design interface specified the use of standard 3/4"-round flanges and access to the mixer block mounting holes at the main- and side-arm flanges. To achieve clearance between the side- and main-arm port flanges, the side-arm power combiner was realized at the interface of a 1:1 to 2:1 transition and a 65° miter was used in the main-arm port. This miter design provides full waveguide-band performance without the discontinuity jutting above the plane of the split-block and minimized the guide lengths for the indicated constrains. The side-arms were realized in 2:1 guide and are combined in a 1:1 guide which is adiabatically transformed to standard guide. This reduces the ohmic loss at room temperature which results from the relatively long waveguide lengths required to mate to the standard 3/4"-round flange. Placing the impedance transformer after the side-arm power combiner relaxes the tolerances required to maintain the phase match before the signals are recombined. The waveguide length required in an optimal symmetric OMT is approximately twice that used in an asymmetric design.

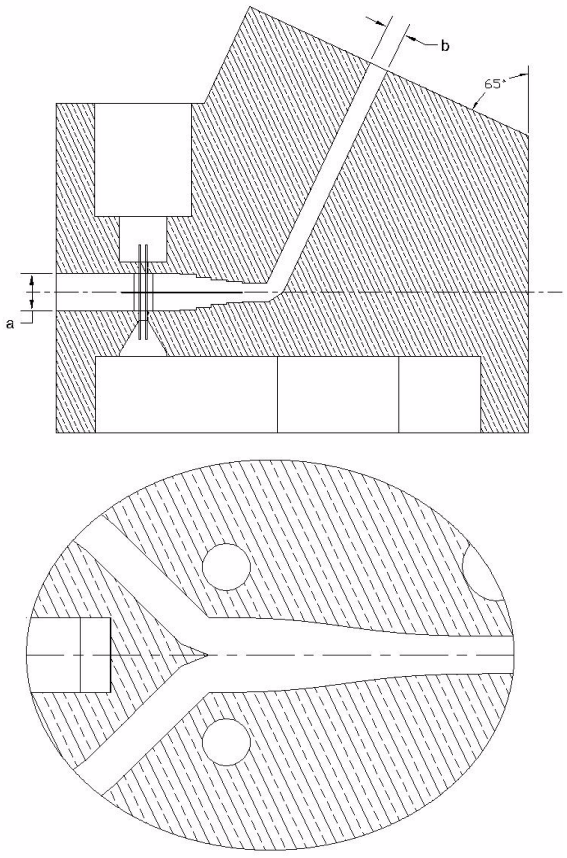

Figure 5: Main-Arm Section of ALMA Band 3 OMT and Side-Arm Power Combiner Detail. Main/Side-Arm ports are WR10.0.

The split-block housing was fabricated out of brass. The main-arm output section was defined by multiple pass EDM (Electric-Discharge-Milling). The septum was made out of beryllium copper stock [24]. The septum is integrated into the 2:1 stepped main-arm transformer. For lower frequency designs, sinuously ground beryllium copper pins [25] have been utilized for the compensation pins. However, for the WR10.0 design, a ~0.1m length of 125µm diameter copper-clad steel magnet wire [26] was threaded through the holes to realize each "pin".

After mating of the block halves with the septum, the pins (wires) were mechanically stabilized by potting with Emerson-Cuming 2850 FT epoxy [27] on one side of the split-block, and trimmed to final length. The resulting configuration is insensitive to variation in applied force to the pins and allows disassembly of the block if desired. All components were gold-plated before assembly.

The performance indicated in Figure 6 is with four pins and the nominal septum placement used to compensate the junction. Measurement frequencies are normalized to the WR10.0 cutoff, f_c = 59.01GHz to facilitate comparison to other components. TRL (Thru-Reflect-Line) was used to calibrate the HP85106D network analyzer. The common-arm termination is a sliding conical load with a return loss ~40dB. The data presented are uncorrected for the resultant measurement errors. The septum used in this measurement set was hand lapped to fit in the split-block housing and was noted to have a slight curvature. Numerical modeling indicates that the dominant effect is a degradation of the isolation. The insertion loss for bright and bondable pure gold are indicated the figure. The design details described here applies specifically to the WR10.0 OMT, however, most aspects readily scale with frequency. Other realizations of these concepts are presented in Figures 7, 8, and 9. The slow ripple across the band in the insertion loss observed in Figure 7 is an example of insufficient septum clamp pressure. We include this data example to assist in integration and test of the structure. In the final assembly this discrepancy was corrected by up-plated with septum gold and the ripple and overall insertion loss levels were reduced.

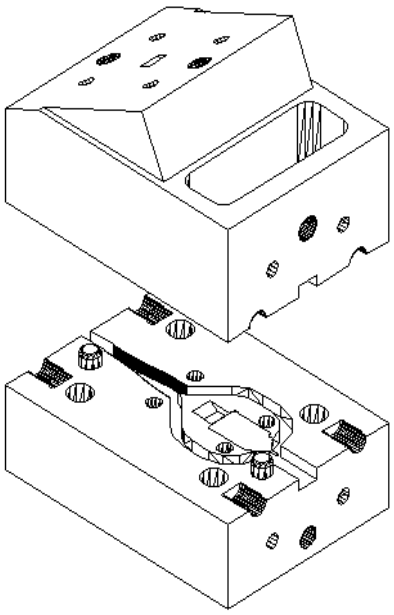

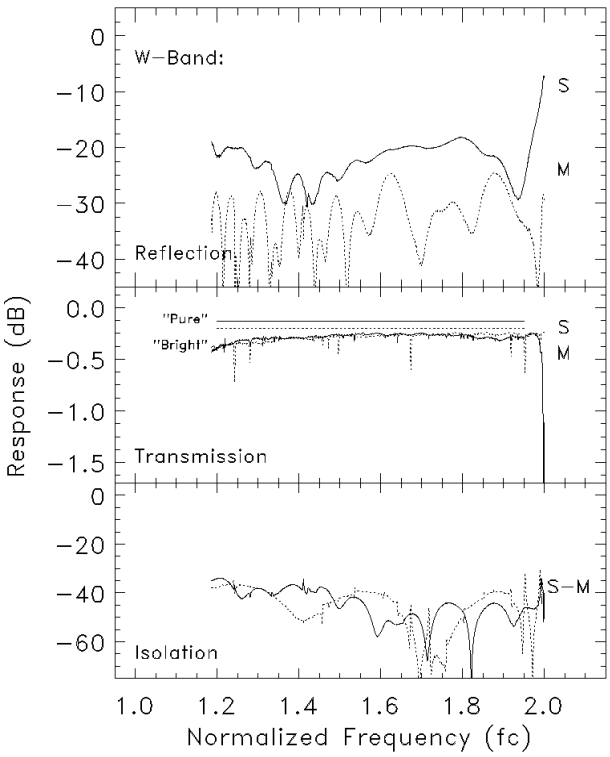

Figure 6: WR10.0 Bøifot Junction OMT (fc=59.01GHz). The solid and dashed lines are respectively the side- and main-arm responses for reflection and transmission. "Pure" and "Bright" indicate the magnitude of the transmission loss with bondable and bright gold plating respectively. The solid isolation line is with a load on the common-arm; the dashed line is with a short on the common-port

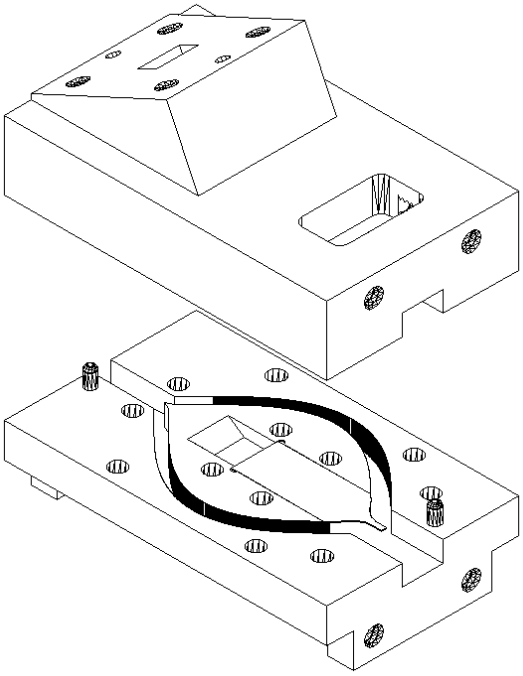

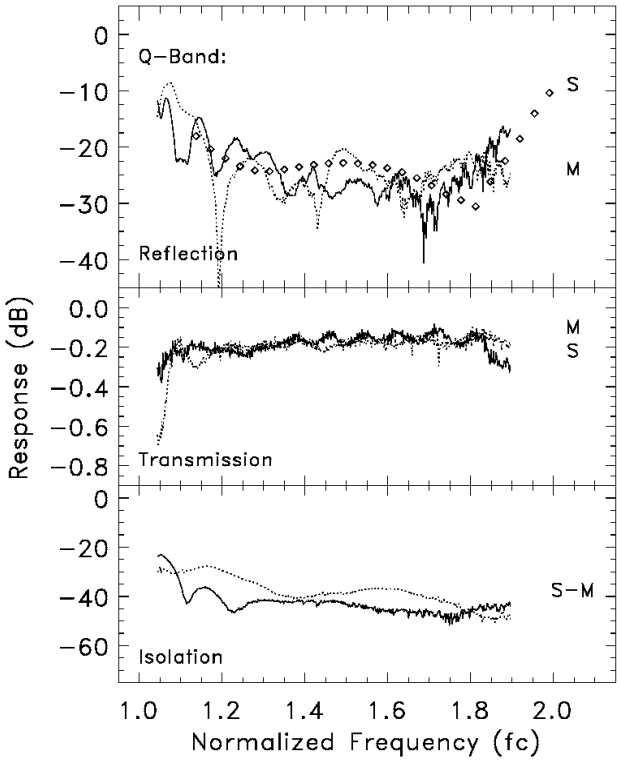

Figure 7: WR22.4 Bøifot Junction OMT (fc=26.35GHz). The solid and dashed lines are respectively the side- and main-arm responses for reflection and transmission. The diamonds are the side-arm modeled response. The split-block is unplated aluminum. The solid isolation line is with a load on the common-arm; the dashed line is with a short on the common-port.

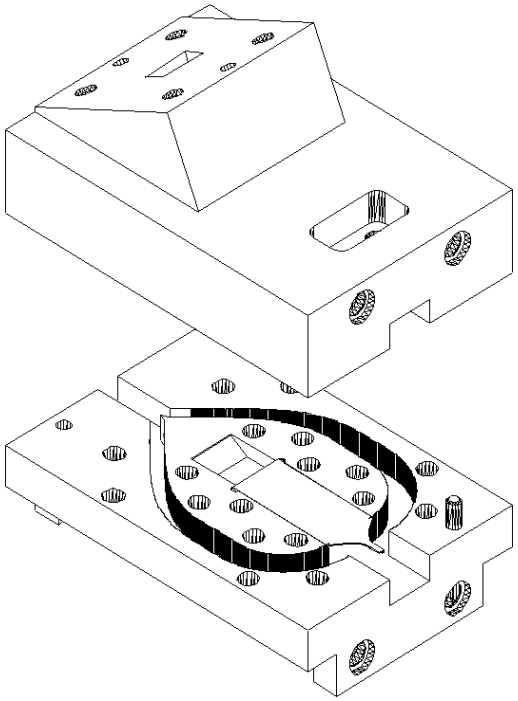

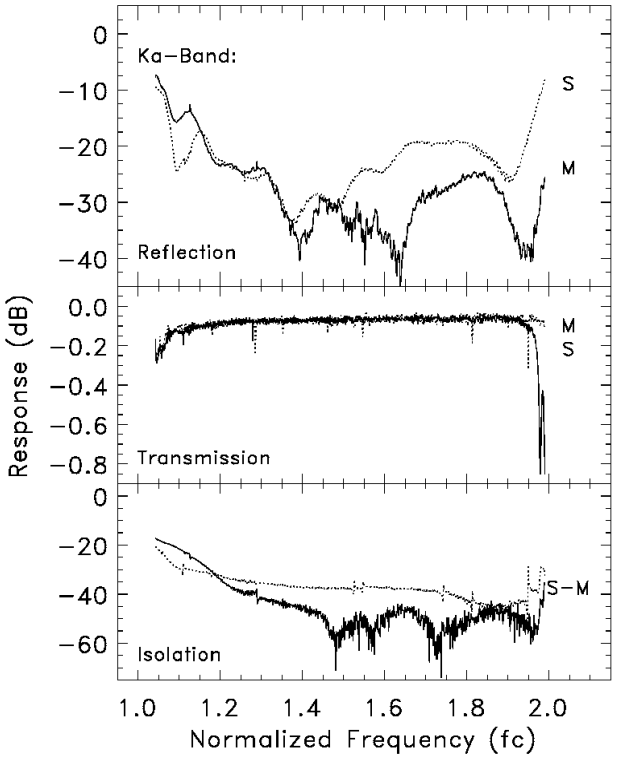

Figure 8: WR28.0 Bøifot Junction OMT (fc=21.08GHz). The solid and dashed lines are respectively the side- and main-arm responses for reflection and transmission. The solid isolation line is with a load on the common-arm; the dashed line is with a short on the common-port

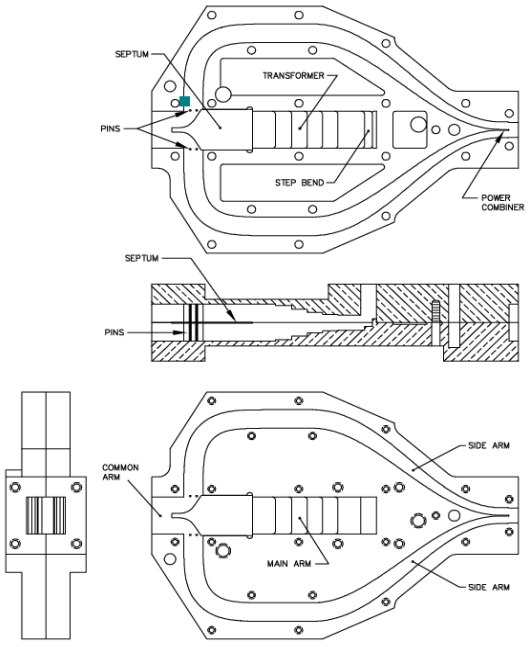

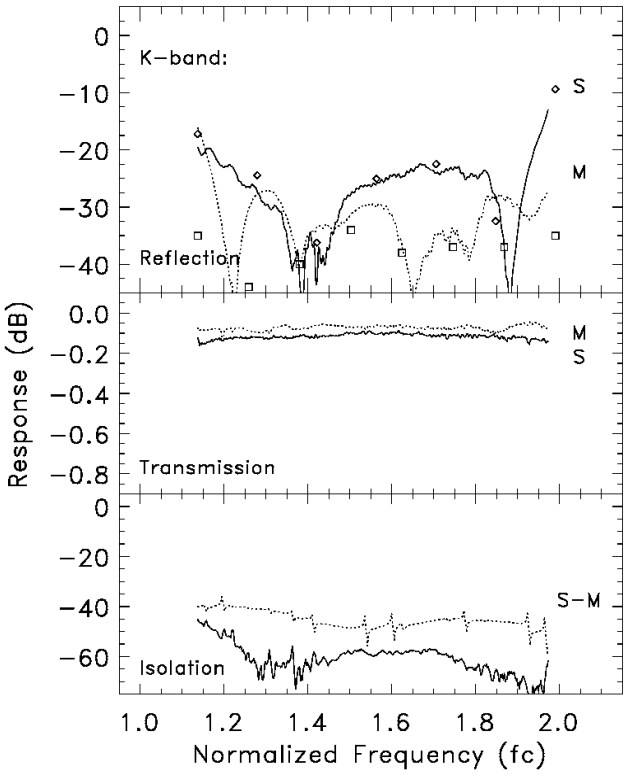

Figure 9: WR42.0 Bøifot Junction OMT (fc=14.07GHz). The solid and dashed lines are respectively the side- and main-arm responses for reflection and transmission. The modeled side-arm response depicted with diamonds; the main-arm response without the miter is indicated with boxes. The solid isolation line is with a load the common-arm; the dashed line is with a short on the common-port.

Wave Band	Output Guides [WR]	Guide Broadwall	Sidearm Angle Junction : Combiner	Power Combiner Transformer Ratio	Flange Geo.	OMT Mass	Split-Block Envelope (length) (width) (height)
K	42.0	10.67 mm (0.420")	π/2 : 0	0.5 : 1.0	22.2 mm (0.875") Square	445 gm	102 x 71 x 23 mm^3
Ka	28.0	7.11 mm (0.280")	π/2 : π/4	0.5 : 1.0	19.1 mm (0.750") Square	210 gm	49 x 32 x 28 mm^3
Q	22.4	5.69 mm (0.224")	π/4 : π/4	0.5 : 1.0	19.1 mm (0.750") Square	45 gm	44 x 28 x 26 mm^3
W	10.0	2.54 mm (0.100")	π/2 : π/4	1.0 : 2.0	19.1 mm (0.750") Round	110 gm	32 x 22 x 28 mm^3

Table 2: NRAO Bøifot Orthomode Junction Packaging and Layout Summary. Note: The Q-band OMT was fabricated as an aluminum split-block. This layout minimizes overall mass and package envelope with standard flange interfaces. Its mass is within ~10% of an off-the-shelf electroformed-copper asymmetric OMT design.

WAVEGUIDE LOSS:

The waveguide loss can be a useful diagnostic of the quality of the split-block mate. Since the side-arm follows an E-plane split, the current density is minimal in the plane of the split-block and the ohmic losses are insensitive to the details of this interface. The observed side-arm losses are consistent with those estimated from the waveguide geometry, plating conductivity, and a correction from the surface roughness [21,28] measured by optical confocal mapping. The main-arm has block split in H-plane and the current density is maximal in the vicinity of the interface. As such, the main-arm loss is sensitive to the quality of the mate achieved between the two halves of the split-block in the presence of the septum. Misalignment of the septum will prevent proper mating of the two blocks and results in a rolling response in the main-arm insertion loss across the waveguide band (see e.g., Figure 7).

With proper alignment of the blocks and the septum, the observed main-arm loss exceeds the theoretical estimate. Investigation of the source of this excess with H-plane split-block samples revealed that this behavior is related to the details of the surface finish and mating pressure achieved at the interface. For a WR10.0 split-block sample, the loss was reduced from ~5 times to within a factor of ~2 of the theoretical for pure gold by increasing the H-plane split-block clamp pressure. The evidence for plastic deformation by defects at the interface guides our physical interpretation of this observation. In effect, the many finite resistance contacts points between the surfaces are reduced by applying sufficient pressure. Use of conductive “gaskets” (e.g., thin foils of copper, indium, and gold) reveal similar results. Pressure sufficient to leave defect imprints on the surface was required to reach the minimal joint loss. Consideration of a choked split-block [29] or a diffusion bond at this interface could eliminate this concern if desired. A portion of the main-arm is realized by multiple pass EDM and the resulting surface roughness is >2μm rms. To achieve the desired finish this section is precision honed which results in a roughness ~0.3μm rms.

The metalization’s conductivity also influences the observed waveguide loss as a function of temperature. The finite conductivity of a metal arises from the scattering of electrons from two sources: 1) localized defects (impurities and geometric) and 2) thermally induced motion of the lattice. Both terms contribute independently to the resistivity (Matthiessen’s rule). For an ordered metal above the Debye temperature the dominant contribution to the resistivity is scattering of electron waves by thermally displaced atoms. The scatting cross-section of the displaced atoms is proportional to the square of the vibration amplitude, which in turn goes at $\sim k_b T_{amb}$ in this limit. As a result, the conductivity improves as the inverse of the

ambient temperature until the elastic scattering limit for the material is reached. In the dirty or disordered alloy limit, little improvement in conductivity with cooling is anticipated (e.g., stainless steel, brass, electro-deposited gold on copper without a diffusion barrier, etc...). We recall small levels of impurities or environmental exposure can have a pronounced effect on the observed ohmic loss [30]. This effect can be seen in Figure 6 where the magnitude of the observed insertion loss with "Bright (hard) and "Pure" (bondable) gold coatings are indicated for the WR10.0 OMT. For guide lengths greater than ~4 times the guide height, the geometry of the resultant hole will shield the guide walls from the plating solution. Use of appropriate fixturing, flanged ends and interior electrode during plating, is recommended to achieve passivation of the waveguide surface with a high quality metal.

For bulk normal-metals such as copper and gold, the improvement in conductivity typically saturates due to inelastic scattering around ~20-to-50K. If we assume that we have a metal with conductivity, σ, the ohmic loss can be computed by standard techniques and will scale as the classical skin depth, $\delta=(2/\mu\sigma\omega)^{1/2}$. As a result, the eddy current losses in the waveguide walls will scale as $\sim T_{amb}^{1/2}$. One estimates a $(30K/300K)^{1/2} \sim 0.3$ reduction in loss in cooling a high purity normal-metal from room temperature. Measurements of the WR10.0 OMT at ~16K (G. Moorey, private communication, CSIRO, 2002) are consistent with this scaling. The contribution to the system temperature due to the ohmic loss is the product of the loss and ambient temperature of the emitter, $\sim \alpha T_{amb}$. As a result, in the Rayleigh-Jeans limit the contribution to the system temperature scales as $\sim T_{amb}^{3/2}$.

Below the elastic scattering limit, reductions in the emission power from the waveguide walls are linear in temperature until influenced by corrections due to the electron mean-free-path in the metal (anomalous skin effect) and photon occupation number (Wien limit). These considerations can be relevant for cryogenic single-mode bolometric detector systems. The presence of ohmic loss infers mode conversion and coupling. As a result, one observes that the dominant limitation to the detector system from the OMT's insertion loss a reduction in the optical efficiency and isolation arising from the residual reactive mismatch. In this limit, minimization of the reactive mismatch is of greater importance than the ohmic loss in the metal surfaces.

MODE CONVERSION:

With a poor match or short on the OMT common-arm, higher-order modes excited by the junction are trapped. In effect, the common-arm input forms a resonant cavity. Since only a portion of the signal is reconverted back into the fundamental mode, at the cavity resonance frequency, the parasitic wave amplitude sharply increases the transmission loss [31,32,33]. The following observations allow the source of the resonance to be identified: 1) When the OMT septum and pins are removed the resonances are not detected; 2) The response above $\sim 1.4 f_c(TE_{10})$ is smooth with a well-matched common-arm termination; 3) Bending the septum tip (or significant asymmetry between the pins) increases the magnitude of isolation resonances. The dominant sensitivity is the deformation of the septum.

The width of the transmission resonances allows the level of mode conversion in the junction to be estimated by considering the ratio of the diverted power to the power in the fundamental mode [34,35],

$$\alpha \approx \frac{\pi}{2}\frac{\Delta f_r}{f_r}(1 - R(\min)) \ ,$$

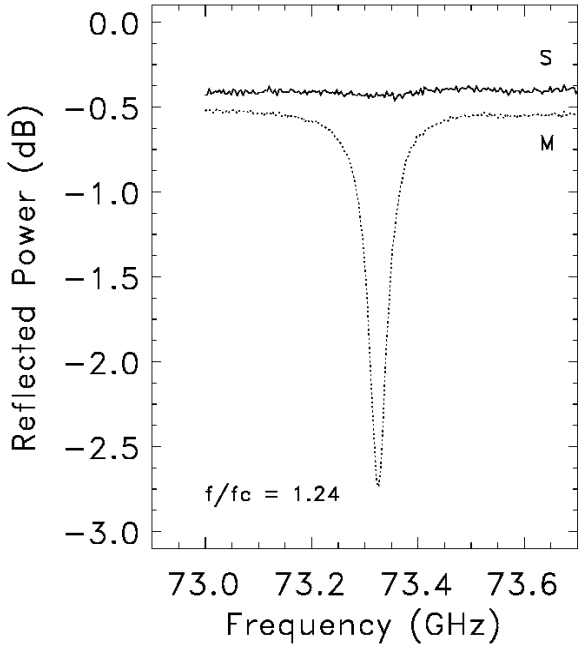

Figure 10: W-Band OMT Main-Arm Transmission Resonance Example. Common-Arm Terminated in Short.

where, f_r is the resonant frequency, Δf_r is the width of the resonance, and R(min) is the depth of the resonance. Referring to Figure 10, we estimate for the WR10.0 OMT a mode conversion level of less than ~28dB. Similar diagnostics are possible by viewing the side/main-arm response with common-arm terminated with a short (crosstalk) and matched load (isolation).

Bending the septum tip has little or no effect on average properties of OMT response, however, it greatly influences the transmission resonance magnitude in the main-arm and the side/main-arm isolation. For example, with the tip deviation equal to the septum thickness, a ~5dB spike observed in return loss corresponds to 10-to-20dB isolation reduction and a transmission resonance spike of ~1dB. With the tip deviation less than ~0.3 of the septum thickness, the return loss spikes could not be detected and transmission resonance amplitude dropped to less than 0.1dB. We find that the deviation of the tip from the plane of the septum should be small compared to the septum thickness to mitigate this effect. The observed performance is consistent with the result obtained with our finite element model of the structure. These considerations suggest that the limiting factor in scaling the structure for use to higher frequencies will be maintaining adequate control over the septum mate to the split-block and its overall camber.

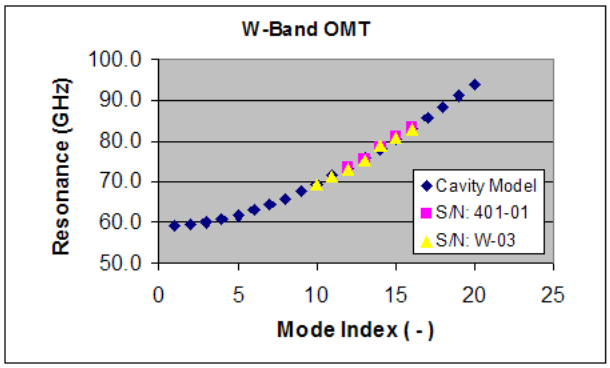

Figure 11: Transmission Resonance Model and Data

Following Montgomery ([21], pp 361-364) we estimate resonant frequency of the trapped modes with the OMT common-arm shorted by considering the cavity formed by the length of the septum and its image. This simple model is compared to the observed response of two different units in Figure 11. This simplified picture would suggest that the septum length should be as short as possible while maintaining the end-to-end isolation for the side-arm. The distance between the septum tip and the common-arm flange should be minimized to increase the spacing between the resonances when the common-arm sees a poor match. Either bending the septum tip or curvature along its width will excite undesired modes which cannot propagate below $1.4f_c$ and show up as loss due to this mechanism.

CONCLUSIONS:

The performances of wideband orthomode junctions are demonstrated for centimeter and millimeter wavebands. An insertion loss <0.2 dB is measured for W-band and improves modestly upon cooling to cryogenic temperatures. Isolation is typically >40 dB, and return loss ~20 dB. Components based upon these designs have been incorporated into state-of-the-art bandband low-noise receivers for radioastronomy. One notes, however, to realize the full potential of this approach for wavelengths less than ~4mm, integration of the OMT structure or use the use of custom waveguide flange interfaces will be of increased importance for low-noise applications. In directly scaling this device to ~1mm, controlling the septum flatness places a potential limit on the control of mode conversion. In this limit, increasing the septum thickness/stiffness, reducing of the tip length, and maintaining an acceptable mate at the split-block interface will be of importance and may limit direct application of this approach.

ACKNOWLEDGMENT:

This work was supported by the VLA Upgrade and ALMA Programs under the National Radio Astronomy Observatory and by the MAP Project under the NASA Office of Space Science. The National Radio Astronomy Observatory is a facility of the National Science Foundation operated under cooperative agreement by Associated Universities, Inc. Discussions with A.R. Kerr, G. Morris, J. Payne, and M. Pospieszalski are gratefully acknowledged by the authors.

APPENDIX A: EVALUATION OF HECKEN TAPER:

The Hecken taper is a near-optimum matching section in the sense that it approaches an "equal-ripple" response without the use of abrupt discontinuities [36]. We follow Grossberg's approach outlined in [37] for derivation of the coefficients necessary for the efficient evaluation of the function required for synthesizing the desired impedance profile [38],

$$G(z,B) = \frac{B}{\sinh(B)} \int_0^z I_0\left(B\sqrt{1-\zeta^2}\right)\, d\zeta$$
$$\equiv \frac{2B}{\sinh(B)}\,\phi(z,B).$$

Substituting the series expansion for a modified Bessel function of order zero, the series is integrated term-by-term. Upon noting that the expression is uniformly convergent on the desired range, -1 < z < +1, one obtains,

$$\phi(z,B) = \sum_{k=0}^{\infty}\left(\frac{B^k}{2^k k!}\right)^2\left(\frac{1}{2}\int_0^z\left(1-\zeta^2\right)^k d\zeta\right)$$
$$= \sum_{k=0}^{\infty} a_k(B)\; b_k(z),$$

where,

$$a_k \equiv \sum_{k=0}^{\infty}\left(\frac{B^k}{2^k k!}\right)^2 = \left(\frac{B}{2k}\right)^2 a_{k-1},$$

and

$$b_k \equiv \frac{1}{2}\int_0^z\left(1-\zeta^2\right)^k d\zeta = \frac{\left(1-z^2\right)^k b_o + 2k\, b_{k-1}}{2k+1}$$

with a_o=1 and b_o=z/2. For completeness, the algorithm used for the evaluation of the Hecken impedance taper is included below:

```
FUNCTION   phi(z_o, b_o)
   real phi, z_o, b_o, a_k, b_k, c_k, f_k, tol
   integer k, k_max
   parameter (k_max=21, tol=1.0e-7)
      a_k=1.
      b_k=z_o/2.
      c_k=b_k
      phi=b_k
        do k=1,k_max
          f_k=k
          c_k=c_k*(1.-z_o**2)
          b_k=(c_k+2.*f_k*b_k)/(2.*f_k+1.)
          a_k=(b_o/2./f_k)**2*a_k
          phi=phi+a_k*b_k
          if(abs(a_k*b_k).lt.tol) return
        end do
     return
   end
```

REFERENCES:

[1] Ragan, G.L., *Microwave Transmission Circuits*, 1948, MIT Radiation Laboratory Series, vol. 9, McGraw-Hill, New York, sections 6-17, 6-18 (narrow band OMTs, turnstile junctions, polarizers).

[2] Harvey, A.F., Microwave Engineering, 1963, Academic Press, New York, pp. 105–107, 119–120, 890, 919–920 (narrow band OMTs, turnstile junctions, polarizers, balanced diplexers).

[3] Smullin, L.D. and Montgomery, C.G., *Microwave Duplexers,* 1948, MIT Radiation Laboratory Series, vol. 14, McGraw-Hill, New York, chapters 7, 8 (di-plexing circuits, turnstile junctions, tee junctions).

[4] Robertson, S.D., "Recent Advances in Finline Circuits," 1956, IRE Trans. Microwave Theory Techniques, vol. 4, no. 4, pp. 263– 267.

[5] Chattopadhyay, G. and Carlstrom, J.E., "Finline Ortho-Mode Transducer for Millimeter Waves," 1999, IEEE Microwave and Guided Wave Letters, vol. 9, no. 9, pp. 339–341.

[6] Skinner, S.J., and James, G.L., "Wide-Band Orthomode Transducers," 1991, IEEE Trans. on Microwave Theory and Techniques, vol. 39, no. 2, pp. 294–300.

[7] Steffe, W., "A Novel Compact OMJ for Ku Band Intelsat Applications," 1995, IEEE Antennas and Propagation Society International Symposium, , Newport Beach, CA, vol. 1, pp. 152–155.

[8] Meyer, M.A. and Goldberg, H.B., "Applications of the Turnstile Junction," 1955, IRE Trans. Microwave Theory and Techniques, vol. 3, no. 6, pp. 40–45.

[9] Gehin, C. and Tourneur, J., "A Wideband Polarization Diplexer Device and an Antenna Associated with a Radar or a Counter-Measure," 1986, UK Patent, GB 2 175 145 A (OMT realized with square-to-ridge waveguide turnstile junction and appropriate power combiners).

[10] Uher, J., Bornemann, J., Rosenberg, U., *Waveguide Components for Antenna Feed Systems: Theory and CAD,* 1993, Artech House, Norwood, MA, section 3.8, pp. 371–445.

[11] Bøifot, A.M., Lier, E., Schaug-Pettersen, T., "Simple and Broadband Orthomode Transducer," 1990, Proc. IEE, vol. 137, no. 6, pp. 396–400; Bøifot, A.M., "Classification of Ortho-Mode Transducers," 1991, European Transactions on Telecommunications and Related Technologies, vol. 2, no. 5, pp. 503–510.

[12] Wollack, E., "A Full Waveguide Band Orthomode Junction," 1996, NRAO, EDIR Memo Series, #303.

[13] Cazzatello, G.F., Barbiero, M., Giglia, C.G.M., Klooster, C.G.M., "Wide-Band Dual-Polarized Feeds," 1996, Workshop on Large Antennas in Radio Astronomy, ESTEC, Noordwijk, Netherlands, pp. 159–171.

[14] Nesti, R., Private Communication, Osservatorio Astrofisico di Arcetri, Firenze, Italy. (Symmetric Ka-band OMT).

[15] Narayanan, G. and Erickson, N.R., "Design and Performance of a Novel Full-Waveguide Band Orthomode Transducer," 2002, 13th Symposium on Space THz Technology, Cambridge MA. (Symmetric W-band OMT)

[16] Hewlett Packard EEsof Division, Hewlett Packard High Frequency Structure Simulator (HFSS), Santa Rosa, CA 95403.

[17] Matthaei, G.L., Young, L., and Jones, E.M.T., *Microwave Filters, Impedance-Matching Networks, and Coupling Structures,* 1964, McGraw-Hill, New York.

[18] Reisdorf, F., "Analysis and Design of Broadband-Matched Multi-Stage Angle Bends in Rectangular Waveguides," 1976, Frequenz, vol. 30, no. 5, pp. 126–131.

[19] Wollack, E., "Notes on Right-Angle-Miter Bends for Standard Rectangular Waveguide," 1995, NRAO, EDTN Memo Series, #172.

[20] Wollack, E., "Simple Split-Block 90-Degree E-Plane Bends for Low Power Applications," 2001, NRAO, EDTN Memo Series, #187.

[21] Montgomery, C.G., Dicke, R.H., Purcell, E.M., *Principles of Microwave Circuits,* 1987, IEE Electromagnetic Waves Series, vol. 25, Peter Peregrinus, London, chapter 12. (First published 1948, MIT Radiation Laboratory Series, Vol. 8, McGraw-Hill, New York.)

[22] De Ronde, F.C., "Full-Band Matching of Waveguide Discontinuities," 1966, G-MTT Digest, p. 208.

[23] Wollack, E., "On the Compensation of E-Plane Bifurcations in Rectangular Waveguides," 1997, NRAO, EDTN Memo Series, #181.

[24] NGK Metal Corp, BeCo shim stock, Elkhart, IN 46516.

[25] Meyer Gauge, sinuously ground hardened BeCu Pins, Windsor, CT 06074.

[26] California Fine Wire, material number 100-058, 125µm diameter, steel full hard steel wire, copper-clad (40% conduction), Grover Beach, CA 93483.

[27] Emerson-Cuming, 2850 FT epoxy, Canton, MA 02021.

[28] Tischer, F.J., "Excess Conduction Losses at Millimeter Wavelengths," 1976, IEEE Transactions on Microwave Theory and Techniques, vol. 24, no. 11, pp. 853–858.

[29] Hesler, J., "A Photonic Crystal Joint (PCJ) for Metal Waveguide," 2001, Microwave Symposium Digest, 2001 IEEE MTT-S, vol. 2 , pp. 783–786.

[30] Shoushanian, H., "Don't Fool with Gold Plate Selection," Electronic Design, 1969, pp. 114–118.

[31] Sporleder, F. and Unger, H.G., "Waveguide Tapers, Transitions, and Couplers," 1979, Peter Peregrinus, Ltd., London, pp. 265–268.

[32] Vaganov, R.B., "The Experimental Analysis of the Electromagnetic Fields in Waveguide Junctions Containing Critical Section," Radio Engineering and Electronics Physics, vol. 5, no. 5, 1960, pp. 31–39.

[33] Vaganov, R.B. and Meriakri, V.V., "Suppression of Resonance Phenomena in Multimode Waveguides," 1960, Radio Engineering & Electronic Physics, vol. 8, pp. 1139–1147.

[34] Davis, I., Chignell, R.J., "Wide Band Orthomode Transducers for Low Noise Applications," 1982, ERA Report No. 82-124, ERA RF Technology Center, Surrey, England.

[35] Meadow, R.G., "An Absorption Resonance Method for Measuring Mode Conversion Coefficients of Overmoded Waveguide Components," 1973, Int. J. Electronics, vol. 34, no. 6, pp. 837–848.

[36] Hecken, R.P., "A Near-Optimum Matching Section Without Discontinuities," 1972, IEEE Transactions on Microwave Theory and Techniques, vol. 20, no. 11, pp. 734–739.

[37] Grossberg, M.A., "Extremely Rapid Computation of the Klopfenstein Impedance Taper," 1968, Proceedings of the IEEE, vol. 56, no. 9, pp. 1629–1630.

[38] Cloete, J.H., "Computation of the Hecken Impedance Function," 1977, IEEE Transactions on Microwave Theory and Techniques, vol. 25, no. 5, p. 440.